Nanoscale Advances

ROYAL SOCIETY OF CHEMISTRY

PAPER

View Article Online
View Journal | View Issue

Cite this: *Nanoscale Adv.*, 2024, **6**, 3220

Low-threshold cavity-enhanced superfluorescence in polyhedral quantum dot superparticles†

Xinjie Li,[ab] Linqi Chen,*[a] Danqun Mao,[c] Jingzhou Li,[d] Wei Xie,[c] Hongxing Dong *[ad] and Long Zhang *[abd]

Due to the unique and excellent optical performance and promising prospect for various photonics applications, cavity-enhanced superfluorescence (CESF) in perovskite quantum dot assembled superstructures has garnered wide attention. However, the stringent requirements and high threshold for achieving CESF limit its further development and application. The high threshold of CESF in quantum dot superstructures is mainly attributed to the low radiation recombination rate of the quantum dot and the unsatisfactory light field limiting the ability of the assembled superstructures originating from low controllability of self-assembly. Herein, we propose a strategy to reduce the threshold of CESF in quantum dot superstructure microcavities from two aspects: facet engineering optimization of quantum dot blocks and controllability improvement of the assembly method. We introduce dodecahedral quantum dots with lower nonradiative recombination, substituting frequently used cubic quantum dots as assembly blocks. Besides, we adopt the micro-emulsion droplet assembly method to obtain spherical perovskite quantum dot superparticles with high packing factors and orderly internal arrangements, which are more controllable and efficient than the conventional solvent-drying methods. Based on the dodecahedral quantum dot superparticles, we realized low-threshold CESF (Pth = 15.6 μJ cm^{-2}). Our work provides a practical and scalable avenue for realizing low threshold CESF in quantum dot assembled superstructure systems.

Received 4th March 2024
Accepted 29th March 2024

DOI: 10.1039/d4na00188e

rsc.li/nanoscale-advances

Introduction

Superfluorescence (SF) is a many-body quantum phenomenon arising from an excited cooperatively coupled ensemble, exhibiting short and intense light.[1–5] Owing to its excellent properties, SF has led to considerable research, ideal for various applications in nanophononics,[6,7] photonic computing,[8] and lasers.[9] Since Kovalenko and coworkers[10] successfully validated the occurrence of SF by assembling simple cubic quantum dots into a three-dimensional ordered cubic superlattice structure, perovskite quantum dots (QDs) have proven to be a promising platform for the physical mechanism research and applications of SF,[11] with large oscillator strengths, high quantum yields, and prolonged coherence times.[12–15]

Numerous studies have been conducted on manipulating and controlling coherent photon bundles or bursts in perovskite systems.[16–22] Combining a quantum ensemble with an optical cavity results in the generation of exciton coherent coupling, giving rise to cavity-enhanced superfluorescence (CESF). CESF facilitates the control of ultrafast radiation of excitonic collective states, and its outstanding performance is expected to be utilized as a quantum switch in quantum communication.[9] It addresses the issue of low efficiency in blue light sources,[23] as well as improving coupling efficiency and monochromaticity issues in laser systems.[9,24] However, the current realization of CESF in trihalide perovskite quantum dot systems faces the problem of high thresholds. The realization of low-threshold CESF is limited by three significant requirements: low nonradiative recombination of quantum dot blocks, regular structure of self-assemblies that can provide good light feedback effect, and high packing factor of quantum dots in assemblies. The inevitable surface defects induced by long-chain organic ligands (oleylamine) on cubic quantum dots lead to high nonradiative recombination.[25] Facet engineering strategies have recently emerged as a focal point of attention and admiration due to the immense potential in modulating the optical properties of quantum dots.[26–28] Replacing cubic

[a]Key Laboratory of Materials for High-Power Laser, Shanghai Institute of Optics and Fine Mechanics, Chinese Academy of Sciences, Shanghai 201800, China. E-mail: chenlq@siom.ac.cn; hongxingd@siom.ac.cn; lzhang@siom.ac.cn

[b]School of Physical Science and Technology, ShanghaiTech University, Shanghai 201210, China

[c]State Key Laboratory of Precision Spectroscopy, School of Physics and Electronic Science, East China Normal University, Shanghai 200241, China

[d]Hangzhou Institute for Advanced Study, University of Chinese Academy of Sciences, No. 1, Sub-Lane Xiangshan, Xihu District, Hangzhou 310024, China

† Electronic supplementary information (ESI) available: Supplementary figures; tables; supplementary note of theoretical model. See DOI: https://doi.org/10.1039/d4na00188e

quantum dots with polyhedral quantum dots for assembly might be a feasible optimization strategy. In addition, recent advances in perovskite quantum dots suggest that programmable collective emission tuning and theoretical framework building require broadening the engineerability of the assembled structure.[29] The uncontrolled morphology of superstructures assembled through the traditional solvent evaporation method impedes the realization and application of low-threshold CESF. For colloidal quantum dot self-assembly, the microemulsion template method has been reported to show high controllability and high yield.[30] Meanwhile, quantum dots with increased number of facets fit well with the spherical microemulsion template, which contributes to realizing the high packing factor of the assemblies.

Here, we present a solution to replace the commonly assembled blocks from cubic to dodecahedral quantum dots and assemble the superstructures with a more controllable assembly method to realize regular morphology that can serve as an optical cavity. Using a modified hot injection method, we synthesized perovskite rhombic dodecahedral quantum dots and investigated their formation mechanism. Through temperature-dependent photoluminescence (PL) measurements, we discovered that dodecahedral quantum dots exhibit smaller electron–phonon coupling compared to cubic quantum dots, leading to smaller nonradiative recombination. Besides, oil-in-oil microemulsion templates were used to efficiently assemble dodecahedral quantum dots into spherical perovskite quantum dot superparticles with a high packing factor and regular morphology, enabling the achievement of low-threshold single-mode CESF at 77 K. Furthermore, we employed time-resolved photoluminescence (TRPL) to analyze the ultrafast optical properties and dynamic processes of blue CESF. The development of low-threshold CESF contributes to advancing the application of perovskite quantum dots in optical communication and ultrafast quantum optics.

Experimental section

Materials

Cesium carbonate (Cs_2CO_3, 99.99%), lead monoxide (PbO, 99.99%), oleic acid (OA, 90%), oleylamine (OAm, 90%), 1-octadecene (ODE, 90%), 008-FluoroSurfactant (008-FS), Fluorinert FC-40, and toluene (95%, anhydrous) were purchased from Sigma-Aldrich. 2-Bromo-1-phenylethanone ($C_6H_5COCH_2Br$, 98%) and methyl acetate ($C_3H_6O_2$, 99.5%, anhydrous) were purchased from Aladdin.

Synthesis and purification of rhombic dodecahedral $CsPbBr_3$ QDs

Rhombic dodecahedral $CsPbBr_3$ QDs were prepared according to the modified literature-reported method. In a nutshell, 0.6 mmol Cs_2CO_3, 9 ml ODE, and 1 ml OA were loaded in a 50 ml three-neck round-bottom flask. The reaction mixture was dried under a N_2 flow at 120 °C for 30 min. Then the temperature of the solution was raised to 150 °C until the solution was clear. Before injection, the Cs-oleate precursors were kept above 100 °C to prevent ODE from solidifying. Next, 0.4 mmol PbO, 1.2 mmol $C_6H_5COCH_2Br$, 2 ml OA, and 10 ml ODE were loaded in another 100 ml three-neck round-bottom flask, deaerated under an N_2 flow at 120 °C for 30 min. Then, 1 ml of OAm was injected into the solution when the temperature was raised to 220 °C. The solution was heated at 220 °C for 10 min to obtain a clear yellow color. After that, 1 ml of the Cs-oleate precursor was injected into the solution quickly, and annealed for 15 min. The reaction mixture was quenched in an ice-water bath until the temperature dropped to room temperature. Subsequently, the crude solution was centrifuged at 9000 rpm for 10 min, and the precipitate was taken and dispersed in toluene. Methyl acetate was added to the dispersion solution and centrifuged again for 5 min. Finally, the precipitate was collected and dispersed in toluene.

Self-assembly of rhombic dodecahedral $CsPbBr_3$ QDs superparticles

For obtaining the best self-assembly, 10 μl 008-FS in FC-40 (5 wt%) was injected into 200 μl neat FC-40, forming 5 wt% 008-FS in FC-40. Then, 20 μl of 12-QDs (10 mg ml^{-1}) in toluene was added into the above solution, vortex mixed for 5 minutes, evaporating at 20 °C for a certain time after which the solvent evaporates completely and the microemulsion droplets shrink to form a spherical superparticles.

Structural and optical characterization

The TEM measurements were performed using a transmission electron microscope (Talos F200X G2) operated at 200 kV. The samples were dropped on clean silicon substrates and then transferred onto a 300 mesh copper TEM grid by allowing the sample to slightly touch the mesh. The SEM images were acquired *via* field-emission scanning electron microscopy (Auriga S40, Zeiss, Oberkochen, Germany). The static XRD patterns were acquired using Cu-Kα radiation (PANalytical Empyrean).

Absorption spectra were recorded using a PerkinElmer UV/VIS/NIR spectrometer (Lambda 750, Villeneuve-d'Ascq, France). PL spectra of $CsPbBr_3$ NC solutions were recorded using a confocal micro photoluminescence system (LabRAM HR Evolution) with a high-numerical-aperture microscope objective (N.A. = 0.5, 50×). The excitation source was a 400 nm femtosecond laser. The temperature-dependent PL experiments were accomplished by placing samples in a Dewar (77-475 K, Janis ST-500, Woburn, MA, USA) with a temperature controller (Cryocon 22C, USA) and liquid N_2 for cooling. In addition, the time-resolved PL spectra of the samples were measured with a streak camera (C10910-05, M10911-01) at 77 K.

Results and discussion

The synthesis method of the rhombic dodecahedral perovskite quantum dots (12-QDs) was modified from the report,[31,32] as detailed in the Experimental section. The shape of the 12-QDs observed *via* high-resolution transmission electron microscopy (HR-TEM) along the [20−1] direction appears as a hexagon

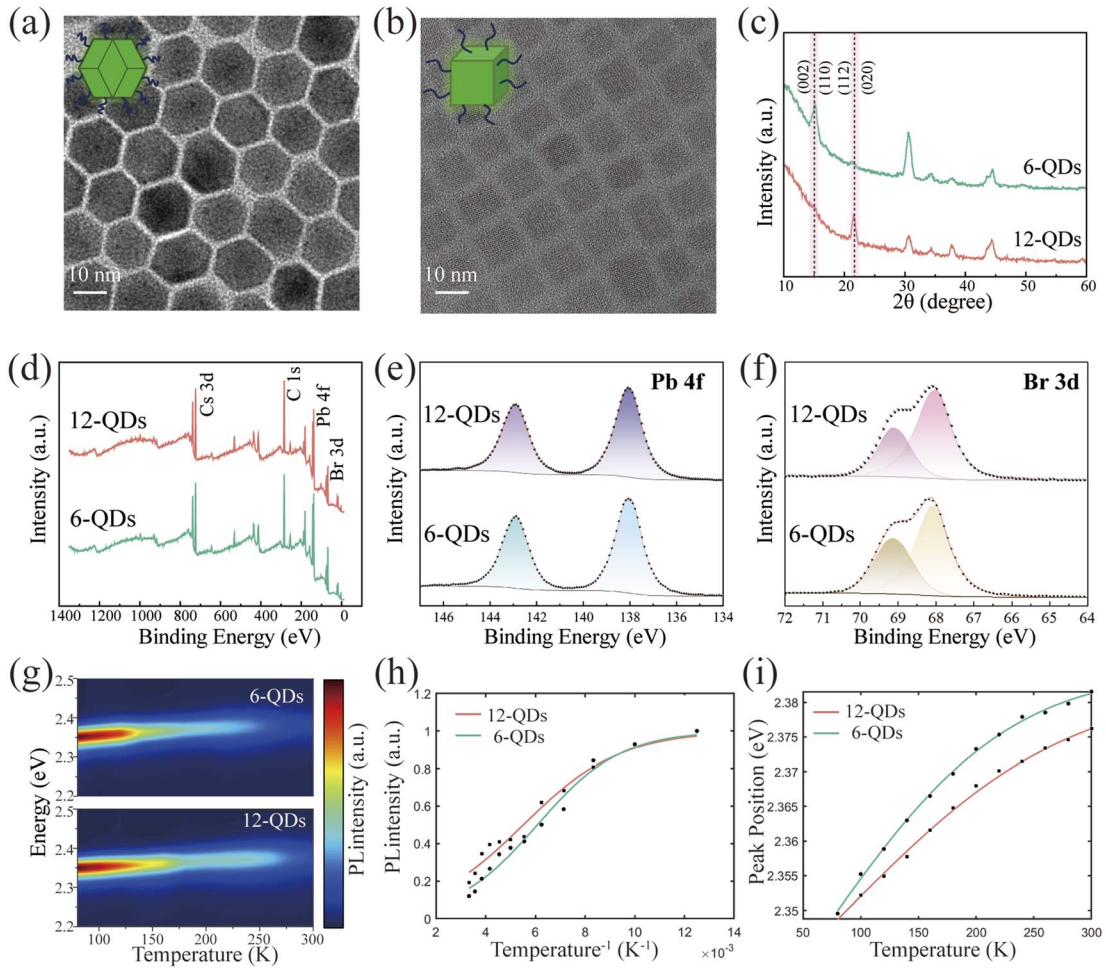

Fig. 1 Structural and optical characterization of 12-QDs and 6-QDs. (a and b) HR-TEM images and the atomic models for 12-QDs and 6-QDs. (c) XRD spectra of 12-QDs and 6-QDs $CsPbBr_3$ perovskite. (d–f) XPS spectra of two perovskite QD films: (d) full spectrum, (e) Pb 4f, and (f) Br 3d. (g–i) Temperature-dependent PL characteristics of 12-QDs and 6-QDs: (g) temperature-dependent PL contour mappings for 12-QDs and 6-QDs, temperature varies in the range of 77 to 300 K, (h) temperature-dependent PL intensity curve and (i) peak position.

(Fig. 1a). The transmission electron microscopy (TEM) images of the 12-QDs along with the particle size distribution plot provide evidence for the monodispersity and size uniformity of our synthesized sample (Fig. S1†). The energy-dispersive X-ray spectroscopy (EDXS) patterns of 12-QDs confirm the uniform distribution of Cs, Pb, and Br elements in space (Fig. S2†). Additionally, the 12-QDs displayed a highly crystalline structure. Based on the Fast Fourier Transform (FFT) patterns obtained from the selected region, the measured *d*-spacing of 4.8 nm^{-1} corresponds to the (200), (020), and (112) series planes of orthorhombic $CsPbBr_3$ (Fig. S3†). To better investigate the properties of the 12-QDs, we synthesized cubic hexahedral quantum dots (6-QDs) with an average size of approximately 10 nm as a control group (Fig. 1b). In contrast to typical syntheses of 6-QDs, the 12-QDs utilize 2-bromo-1-phenylethanone as the bromide source, an α-halo ketone that helps to release bromide in the presence of alkylamine during the reaction and slows down the reaction progress.[33] The generation of tertiary ammonium ions was verified through Fourier transform infrared spectroscopy (FTIR), as detailed in Fig. S4.† The rhombic dodecahedral morphology of 12-QDs arises from the *in situ* generation of tertiary ammonium ions.[34] The (200), (020), and (112) crystal planes of $CsPbBr_3$ are opened and stabilized by successive nucleophilic substitution reactions (SN_2) induced by the release of HBr from 2-bromo-1-phenylethanone. Meanwhile, oleylamine-modified $CsPbBr_3$ stabilizes the (100) and (002) crystal planes. Powder X-ray diffraction (XRD) patterns of both 6-QDs and 12-QDs exhibit orthorhombic phases belonging to the *Pbnm* space group. The XRD pattern clearly shows that the diffraction peak intensities corresponding to the (112) and (020) faces of the 12-QDs are much more pronounced than the 6-QDs (Fig. 1c). All these observations affirm that 12-QDs maintain a polyhedral morphology, consistent with previous reports.[34] We further explored the surface chemical states of 12-QDs using X-ray electron spectroscopy (XPS) (Fig. 1d–f). The Pb 4f and Br 3d curves of 12-QDs exhibit no pronounced binding energy shift compared to 6-QDs, suggesting that 12-QDs have the same stable surface state as 6-QDs, with the ligand firmly bound to the quantum dot surface.

In addition, we also explored the optical properties of the 12-QDs. A clear exciton absorption peak was observed at 511 nm in the typical UV-visible absorption spectrum of $CsPbBr_3$ 12-QDs, indicating the good stability of 12-QDs (Fig. S5†). Additionally, we focus on observing how the nonradiative recombination of 12-QDs changes with temperature. Thermally activated depopulation at the exciton level and enhanced activation of nonradiative recombination from exciton–phonon coupling are the main reasons for temperature-induced photoluminescence (PL) quenching.[35] We conducted temperature-dependent PL measurements to examine the exciton–phonon coupling strength variation with temperature. The temperature-dependent PL contour mappings are shown in Fig. 1g (temperature varies from 77 to 300 K). We have summarized and fitted these temperature-dependent data (Fig. 1h, i and S6†). The physical parameter data obtained from fitting the temperature-dependent PL experimental data can be found in the ESI (Table S1†). Notably, the higher peak intensity at the same temperature and the smaller peak energy blueshifts with temperature changes both demonstrate that 12-QDs exhibit superior optical stability compared to 6-QDs. The corresponding peak intensity data *versus* temperature can be fitted with the following Arrhenius equation (eqn (1)), which is commonly applied to semiconductor luminescent materials[36] (Fig. 1h),

$$I(T) = \frac{I_0}{1 + A\mathrm{e}^{-\frac{E_B}{K_B T}}} \quad (1)$$

$I(T)$ and $I(0)$are the PL intensities at the temperatures T K and 0 K, A is a constant, K_B is the Boltzmann constant, and E_B is the exciton binding energy.[37] The fitting results show that the exciton binding energy of 12-QDs (70.83 meV) is smaller than that of 6-QDs (82.96 meV). From the fitting results, the exciton binding energy of 12-QDs was reduced by 17% compared to 6-QDs, which corresponds to a weaker exciton–phonon (EP) coupling of 12-QDs.

The PL peak energy *versus* temperature profile can be fitted with the thermal expansion (TE) and EP interaction equations.[38] TE and EP coupling both simultaneously affect the band gap. The band gap and PL peak energy blueshift of both quantum dots decreases with increasing temperature (Fig. 1i). The temperature-dependent band gap can be described by eqn (2).[39]

$$E_g(T) = E_0 + A_T T - A_{EP}\frac{2}{\mathrm{e}^{\frac{\hbar\omega}{K_B T}} - 1} + 1 \quad (2)$$

where E_0 is the normalized band gap, A_T and A_{EP} denote the thermal expansion coefficient and electron–phonon coupling coefficient of the band gap, respectively. At low temperatures, EP coupling is negligible due to the small number of optical phonons. As the temperature rises, the optical phonon modes become more populated, and the energy contribution to the bandgap is negative, so that a progressively smaller amount of blueshift change in the peak position is observed. Besides, the calculated value of A_{EP} for 12-QDs was observed to be smaller than that of 6-QDs.

In addition, excitons and thermally induced phonons have a significant impact on the full width at half maximum (FWHM) of the PL peak when the temperature rises, so we can utilize the characteristics of temperature-dependent FWHM to unveil the strength of EP coupling (Fig. S6†). The fitting equation can be described by a sum of three types of broadening contribution (eqn (3))[40]

$$\Gamma(T) = \Gamma_{inh} + \Gamma_{AC} T + \Gamma_{LO}\left(\frac{1}{\mathrm{e}^{\frac{E_{LO}}{K_B T}} - 1}\right) \quad (3)$$

Γ_{inh} denotes the temperature-independent intrinsic nonuniform linewidth caused by sample inhomogeneity, Γ_{AC} is the acoustic phonon–exciton interaction coefficient,[41] Γ_{LO} is the longitudinal optical phonon–exciton coupling coefficient,[42] and E_{LO} is the optical phonon energy.[41] The fitting parameters are summarized in the ESI (Table S1†). The Γ_{inh} value of 12-QDs is lower than that of 6-QDs, indicating the good shape and dimensional homogeneity of 12-QDs.[43] From the above, we can conclude that 12-QDs have smaller EP interactions, which ultimately lead to smaller nonradiative recombination coefficients. The utilization of the assembly building blocks with low nonradiative recombination lays the foundation for achieving lower threshold CESF.

The versatile surface chemistry of colloidal quantum dots offers numerous avenues for manipulating their process of assembly. In order to better assemble the quantum dots into the regular optical cavity structure, we employed the oil-in-oil microemulsion template method to self-assemble 12-QDs.[30] Fig. 2a illustrates the schematic diagram of the self-assembly process. To assemble 12-QDs into a spherical structure, a solution of 12-QDs dispersed in toluene was dropped into the fluorinated oil. Then a stable emulsion was formed through vigorous vortex mixing. As toluene continuously volatilized, the microemulsion droplets contracted, leading to densification and self-assembly of perovskite quantum dots in the solvent due to the interfacial tension. This process resulted in droplet-shaped superparticles with high internal order. The edge dimension of the quantum dots we selected for self-assembly was about 12 nm (Fig. 2b). We selected samples assembled for 2–3 days for morphological characterization. In the HAADF-STEM image of the partially assembled superparticles, ordered arrangements of quantum dots can be observed (Fig. 2c). The selected area Fourier transform pattern and the electron diffraction patterns further confirm the internal order of the assembly structure (Fig. 2d top inset, Fig. S7†). The superparticle assembled for 7 days exhibited a high packing factor and regular shape, conducive to the optical feedback essential for laser operation. By controlling the size of the microemulsion droplets and the concentration of the quantum dot solution, the spherical superparticle structures can range from 400 nm to 4 μm in diameter. The EDS pattern of the assembled structure affirms the elemental composition of the self-assembled superlattice, with Cs, Pb, and Br uniformly distributed in space (Fig. 2f). Additionally, we confirmed the increase in carrier delocalization through the PL spectra of 12-QDs and superparticles (Fig. 2g). While the emission center wavelength of quantum dots is around 519 nm, the emission spectrum of

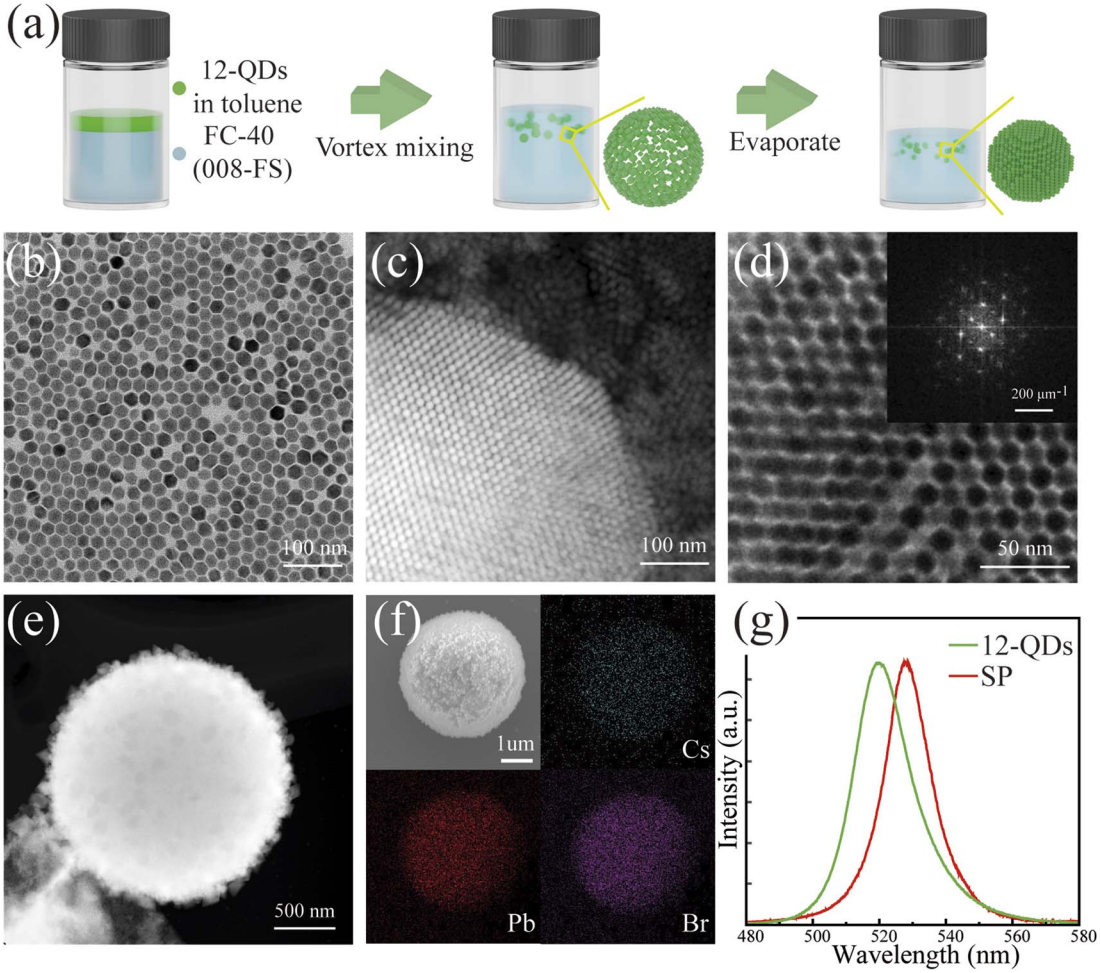

Fig. 2 The assembly process, morphological and optical characterization of spherical superparticle. (a) Schematic diagram of spherical superparticles by the microemulsion template method. (b) TEM image of monodisperse quantum dots for assembly (in toluene). (c) HAADF-STEM image of the semi-assembled structure with a regular periodic arrangement. (d) TEM pattern of the semi-assembled structure. Top inset: selected area Fourier transform pattern. (e) HAADF-STEM image of a spherically shaped regular superparticle. (f) EDXS elemental mapping of a spherical superparticle, displaying its uniform elemental composition. (g) PL spectra of uncoupled 12-QDs and a coupled spherical superparticle.

the superparticle is red-shifted to approximately 528 nm. This shift is attributed to the overlap of the wavefunctions of quantum dots, which results from increased quantum dot coupling at short distances, and the splitting of electronic states into new energy bands.[44,45]

The high gain density resulting from the regular structure of self-assemblies, which provides a good light feedback effect, combined with the high packing factor of quantum dots in assemblies, makes the assembled spherical superparticle an ideal material for realizing CESF. In the preceding section of the article, we demonstrated that 12-QDs exhibit lower nonradiative recombination compared to 6-QDs. We conducted experiments to investigate whether the self-assembled superparticles formed by 12-QDs for use as optical cavities have lower thresholds than those formed by conventional 6-QDs. We achieved pure green CESF at 530.7 nm using a homemade confocal microscope concentrator system, with a 400 nm femtosecond laser as the excitation source at 77 K. And the experimental setup is shown in Fig. S8.† We investigated the relationship between PL and pump power. The PL spectra show a transition from spontaneous to excited radiation as the pump density increases (Fig. 3a). At low pump density, a broad SF peak is observed at 527 nm, and with the increase of pump density, a distinctive small spike emerges on the SF background, signifying the realization of CESF. The typical *S*-curve of superparticles describes the nonlinear relationship between PL intensity and pumping density (Fig. 3d upper part). When the pump density reaches 15.6 μJ cm^{-2}, CESF occurs, and the FWHM narrows down to 0.37 nm. The peak value of the CESF can be fitted to the Lorentz function, corresponding to the quality factor calculation formula $Q = \lambda/\delta\lambda$, yielding $Q = 1450$ (Fig. 3b). Moreover, with the increase in density, the FWHM is slightly broadened, possibly due to excitation-induced heating. To further investigate the stability of CESF generated by spherical superparticles, the sample was continuously pumped with a pulsed laser (pumping density of 1.3 Pth). The PL intensity *versus* pumping

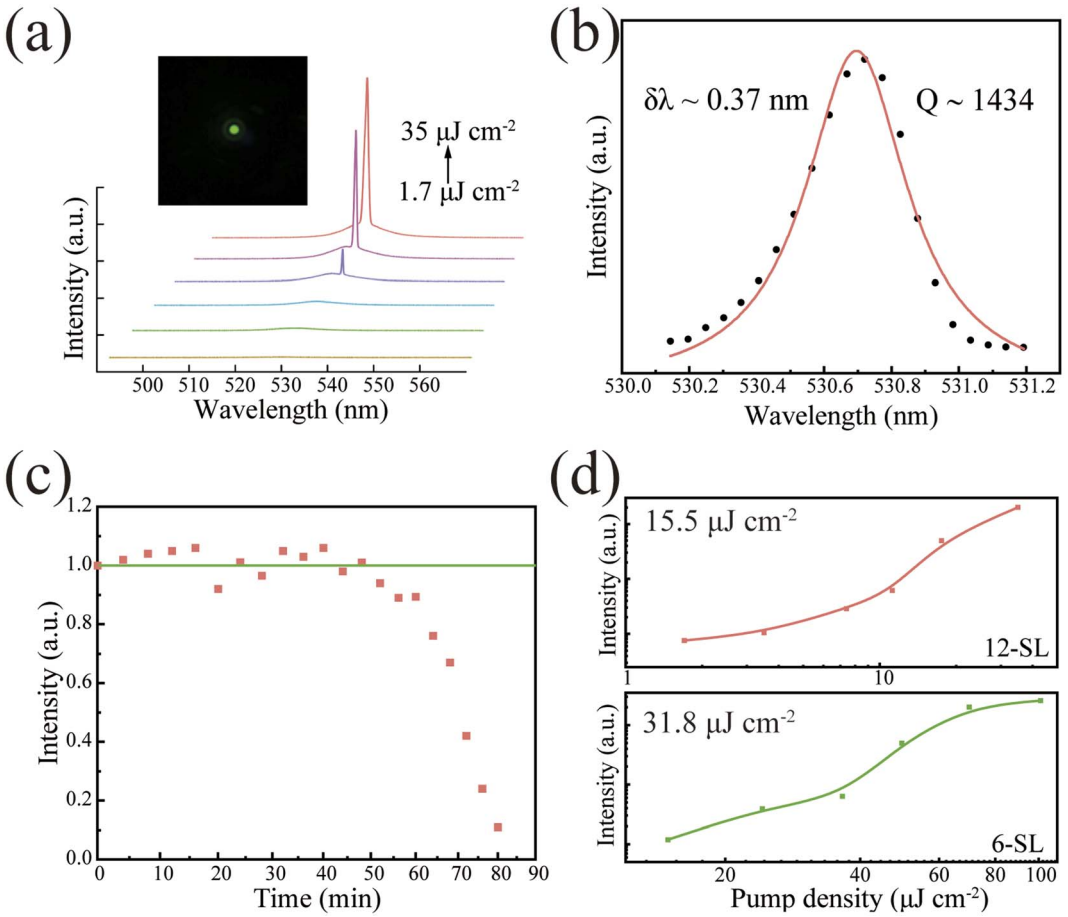

Fig. 3 CESF in a spherical superparticle assembled with 12-QDs. (a) Power-dependent emission spectra of a typical spherical $CsPbBr_3$ superparticle; top inset: the corresponding fluorescence images. (b) Lorentz fitting of a CESF peak; FWHM ($\delta\lambda$) ≈ 0.37 nm, Q factor ≈ 1434. (c) Real-time-integrated emission intensity variation with pumping time, the stable intense output can be maintained for ≈40 min. (d) CESF threshold profiles of the spherical superparticle assembled with 12-QDs and cubic superparticles assembled with 6-QDs.

time curves showed that the stabilized intense light could be continuously output for more than 40 min which verified the high stability of CESF (Fig. 3c). As a comparison, we assembled 6-QDs using the solvent evaporation method. The excitation power-dependent PL spectra of the structure are shown in Fig. S9.† Compared to the cubic superstructure, the gain threshold for CESF in this spherical superparticles was reduced by 50% (Fig. 3d). The previous reports on CESF with a femtosecond-pulsed laser are combined in Table S2.†

Based on the preceding analysis, we attribute the reduction in threshold primarily to improvements in two aspects. Firstly, the utilization of 12-QDs self-assembled building blocks with lower EP coupling. Lower EP coupling implies a reduced nonradiative recombination. The reduction in the portion of excitons losing energy in a nonradiative manner makes achieving a lower threshold for CESF more likely. In addition, the use of oil-in-oil microemulsion templates helps to enhance the stacking factor and control the morphology of the assembled structure by encapsulating droplets. In this context, the superparticles function both as a gain medium and a feedback cavity, effectively enhancing the coupling effect and resulting in a low-threshold CESF. Moreover, the microemulsion template method offers better control over the assembly size of the structure, thereby facilitating further investigation into the structure of perovskite superparticles. This also marks the first utilization of halide perovskite dodecahedral quantum dots to synthesize spherical superparticles. This achievement holds significance in expanding the scope of achievable nanocrystal arrangements in experiments and controlling the self-assembly to synthesize microstructures with desired physicochemical properties.[46]

It is crucial to highlight that CESF has similar characteristics to the optical signals emitted by ordinary lasers in semiconductor microcavities, but they are fundamentally different.[9] In the assembled superparticle, dense excitons exist in a collective quantum state, distinct from the ordinary thermal gas found in classical semiconductor laser systems.[47] CESF originates from a cooperative dipole ensemble. In a cooperative dipole ensemble, the system rapidly dissipates all the in-phase dipoles after emitting the pulse, while the dissipating components of the dipoles slowly radiate in a non-ensemble manner. This contrasts with the excited radiation of thermal excitons in conventional semiconductor lasers, which depends on the particle number inversion conditions. In traditional lasers,

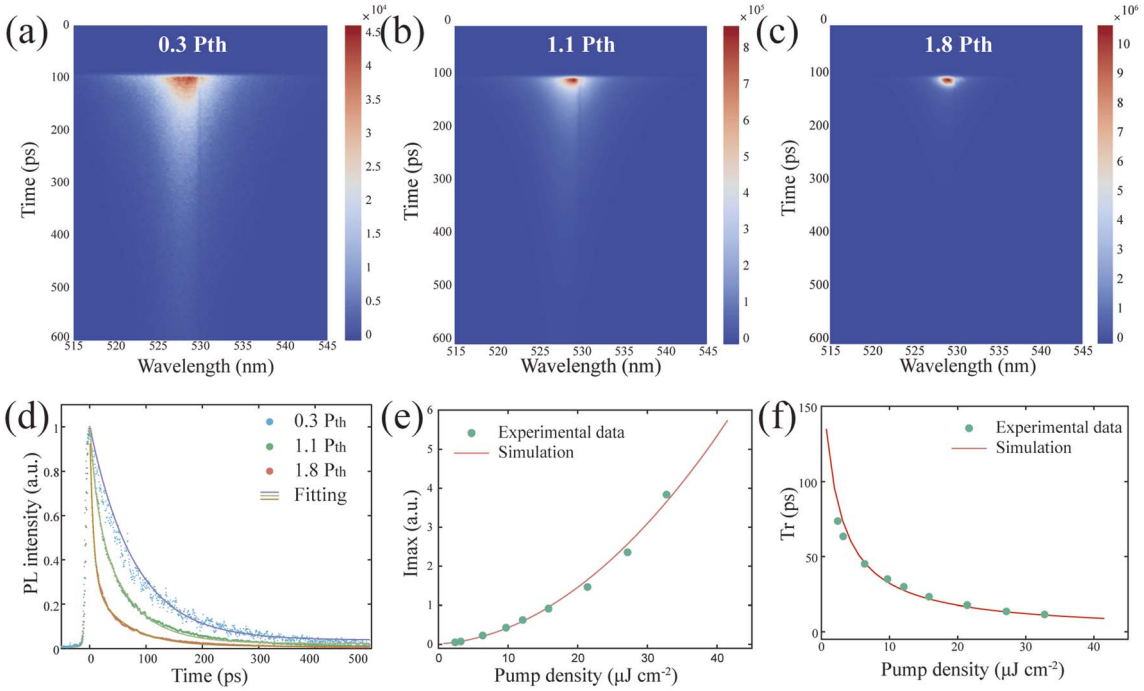

Fig. 4 Ultrafast dynamic analysis of CESF at different pumping densities. (a–c) Streak camera image of SF at different excitation densities: (a) 0.3 Pth. (b) 1.1 Pth. (c) 1.8 Pth. (d) TRPL decay curves under different pumping densities. (e) The relationship curve between the peak intensity of (I_{max}) the signal and the excitation power density. (f) The relationship curve between the radiative time (t_r) of the signal and the excitation power density.

a large number of residual carriers continue emitting slower spontaneous radiation even after the laser is emitted. To further confirm CESF production, experiments were conducted using pump pulses with different time intervals and power densities to examine residual excitons after the fast radiation process, as illustrated in Fig. S10,† providing additional evidence for the production of CESF in spherical superparticles.

To deeply explore the dynamics of laser emission, we investigated the ultrafast optical properties of CESF produced by the spherical superparticles using a 400 nm femtosecond pulsed laser and time-resolved fluorescence spectroscopy (TRPL). By adjusting the excitation density of the streak camera, we recorded the variation of PL intensity over time at different densities (Fig. 4a–c). As the pump density increased, the intensity at the resonance wavelength rapidly rose, accompanied by a sharp decrease in emission bandwidth and decay lifetime, resulting in the observation of a spot at high pump excitation, whereas at low pumping density, the PL decay curve is fitted by a single exponential function, indicating that most of the excitons are coupled together; when the pumping density reaches the threshold, the PL decay curve is fitted by a double exponential function, at which time the carrier lifetime decreases to the picosecond order (Fig. 4d). The detailed fitting parameters of the PL attenuation curves at different pump densities can be found in Table S3.† The radiation time (t_r) and the FWHM of the dynamic PL peak decrease rapidly with increasing pump density. At the same time, the dynamic spotlight peak intensity (I_{max}) increases nonlinearly during the corresponding process, both of which are well simulated with the theoretical model (Fig. 4e and f) (ESI Note 1†).

Conclusions

In conclusion, we successfully synthesized rhombic dodecahedral $CsPbBr_3$ quantum dots, which exposed and stabilized new facets on their surface through the *in situ* generation of tertiary ammonium ions, aligning with prior findings. The stability performance of 12-QDs is equivalent to that of 6-QDs $CsPbBr_3$. Through temperature-dependent PL spectra analyses, we verified that 12-QDs exhibit reduced EP coupling and superior suppression of nonradiative recombination compared to 6-QDs, resulting in a lower threshold. Meanwhile, we improved the self-assembly method, employing the oil-in-oil microemulsion templating to assemble spherical superparticles with a heightened packing factor and more controllable sizes. This method achieved a low-threshold CESF compared to the structure assembled by 6-QDs modified with oleylamine ligands. Furthermore, we delved into the ultrafast optical properties of the spherical superparticles using TRPL, revealing the dynamic characteristics of CESF. By reducing the nonradiative recombination of the assembly building block and enhancing the self-assembly structure to achieve better coupling between the optical cavity with quantum dots, the challenge of achieving low-threshold CESF has been addressed. Notably, this marks the first utilization of 12-QDs to assemble spherical superparticles, expanding the range of building blocks available for perovskite self-assembly. This study introduces a novel approach to realizing low-threshold emission, with potential applications in optical communication and ultrafast light sources. Moreover, it holds significance in controlling the self-

assembly process to synthesize microstructures with desired physicochemical properties, thereby expanding the applications of perovskite quantum dots in optoelectronic devices.

Author contributions

Xinjie Li: conceptualization, methodology, investigation, visualization, writing – original draft, writing – review and editing. Linqi Chen: methodology, data curation, writing – review and editing. Danqun Mao: formal analysis and investigation. Jingzhou Li: writing – review and editing. Wei Xie: funding acquisition and resources. Hongxing Dong: funding acquisition, project administration and resources. Long Zhang: funding acquisition, project administration and resources.

Conflicts of interest

There are no conflicts to declare.

Acknowledgements

The authors acknowledge the support from the National Natural Science Foundation of China (No. 61925506, 12374297, 62305078) and Hangzhou Science and Technology Bureau of Zhejiang Province (No. TD2020002). H. D. acknowledges the Academic/Technology Research Leader Program of Shanghai (23XD1404500).

Notes and references

1 R. Bonifacio and L. A. Lugiato, *Phys. Rev. A: At., Mol., Opt. Phys.*, 1975, **11**, 1507–1521.
2 M. F. H. Schuurmans and D. Polder, *Phys. Lett. A*, 1979, **72**, 306–308.
3 R. H. Dicke, *Phys. Rev.*, 1954, **93**, 99–110.
4 G. T. Noe Ii, J.-H. Kim, J. Lee, Y. Wang, A. K. Wójcik, S. A. McGill, D. H. Reitze, A. A. Belyanin and J. Kono, *Nat. Phys.*, 2012, **8**, 219–224.
5 K. Cong, Q. Zhang, Y. Wang, G. T. Noe, A. Belyanin and J. Kono, *J. Opt. Soc. Am. B*, 2016, **33**, C80–C101.
6 M. Biliroglu, G. Findik, J. Mendes, D. Seyitliyev, L. Lei, Q. Dong, Y. Mehta, V. V. Temnov, F. So and K. Gundogdu, *Nat. Photonics*, 2022, **16**, 324–329.
7 C.-Y. Chan, M. Tanaka, Y.-T. Lee, Y.-W. Wong, H. Nakanotani, T. Hatakeyama and C. Adachi, *Nat. Photonics*, 2021, **15**, 203–207.
8 C. S. Muñoz, E. del Valle, A. G. Tudela, K. Müller, S. Lichtmannecker, M. Kaniber, C. Tejedor, J. J. Finley and F. P. Laussy, *Nat. Photonics*, 2014, **8**, 550–555.
9 C. Zhou, Y. Zhong, H. Dong, W. Zheng, J. Tan, Q. Jie, A. Pan, L. Zhang and W. Xie, *Nat. Commun.*, 2020, **11**, 329.
10 G. Rainò, M. A. Becker, M. I. Bodnarchuk, R. F. Mahrt, M. V. Kovalenko and T. Stöferle, *Nature*, 2018, **563**, 671–675.
11 D. D. Blach, V. A. Lumsargis, D. E. Clark, C. Chuang, K. Wang, L. Dou, R. D. Schaller, J. Cao, C. W. Li and L. Huang, *Nano Lett.*, 2022, **22**, 7811–7818.
12 X. He, Y. Qiu and S. Yang, *Adv. Mater.*, 2017, **29**, 1700775.
13 M. J. Jurow, T. Morgenstern, C. Eisler, J. Kang, E. Penzo, M. Do, M. Engelmayer, W. T. Osowiecki, Y. Bekenstein, C. Tassone, L.-W. Wang, A. P. Alivisatos, W. Brütting and Y. Liu, *Nano Lett.*, 2019, **19**, 2489–2496.
14 H. Utzat, W. Sun, A. E. K. Kaplan, F. Krieg, M. Ginterseder, B. Spokoyny, N. D. Klein, K. E. Shulenberger, C. F. Perkinson, M. V. Kovalenko and M. G. Bawendi, *Science*, 2019, **363**, 1068–1072.
15 F. P. García de Arquer, D. V. Talapin, V. I. Klimov, Y. Arakawa, M. Bayer and E. H. Sargent, *Science*, 2021, **373**, eaaz8541.
16 I. Cherniukh, T. V. Sekh, G. Rainò, O. J. Ashton, M. Burian, A. Travesset, M. Athanasiou, A. Manoli, R. A. John, M. Svyrydenko, V. Morad, Y. Shynkarenko, F. Montanarella, D. Naumenko, H. Amenitsch, G. Itskos, R. F. Mahrt, T. Stöferle, R. Erni, M. V. Kovalenko and M. I. Bodnarchuk, *ACS Nano*, 2022, **16**, 7210–7232.
17 F. Krieg, P. C. Sercel, M. Burian, H. Andrusiv, M. I. Bodnarchuk, T. Stöferle, R. F. Mahrt, D. Naumenko, H. Amenitsch, G. Rainò and M. V. Kovalenko, *ACS Cent. Sci.*, 2021, **7**, 135–144.
18 Y. Tong, E.-P. Yao, A. Manzi, E. Bladt, K. Wang, M. Döblinger, S. Bals, P. Müller-Buschbaum, A. S. Urban, L. Polavarapu and J. Feldmann, *Adv. Mater.*, 2018, **30**, 1801117.
19 A. Jana, A. Meena, S. A. Patil, Y. Jo, S. Cho, Y. Park, V. G. Sree, H. Kim, H. Im and R. A. Taylor, *Prog. Mater. Sci.*, 2022, **129**, 100975.
20 Z. Liu, X. Qin, Q. Chen, T. Jiang, Q. Chen and X. Liu, *Adv. Mater.*, 2023, **35**, 2209279.
21 Y. Zhong, C. Zhou, L. Hou, J. Li, W. Xie, H. Dong and L. Zhang, *Adv. Opt. Mater.*, 2022, **10**, 2102290.
22 J. Liu, X. Zheng, O. F. Mohammed and O. M. Bakr, *Acc. Chem. Res.*, 2022, **55**, 262–274.
23 L. Chen, D. Mao, Y. Hu, H. Dong, Y. Zhong, W. Xie, N. Mou, X. Li and L. Zhang, *Adv. Sci.*, 2023, **10**, 2301589.
24 H. Chang, Y. Zhong, H. Dong, Z. Wang, W. Xie, A. Pan and L. Zhang, *Light: Sci. Appl.*, 2021, **10**, 60.
25 A. Dey, J. Ye, A. De, E. Debroye, S. K. Ha, E. Bladt, A. S. Kshirsagar, Z. Wang, J. Yin, Y. Wang, L. N. Quan, F. Yan, M. Gao, X. Li, J. Shamsi, T. Debnath, M. Cao, M. A. Scheel, S. Kumar, J. A. Steele, M. Gerhard, L. Chouhan, K. Xu, X.-g. Wu, Y. Li, Y. Zhang, A. Dutta, C. Han, I. Vincon, A. L. Rogach, A. Nag, A. Samanta, B. A. Korgel, C.-J. Shih, D. R. Gamelin, D. H. Son, H. Zeng, H. Zhong, H. Sun, H. V. Demir, I. G. Scheblykin, I. Mora-Seró, J. K. Stolarczyk, J. Z. Zhang, J. Feldmann, J. Hofkens, J. M. Luther, J. Pérez-Prieto, L. Li, L. Manna, M. I. Bodnarchuk, M. V. Kovalenko, M. B. J. Roeffaers, N. Pradhan, O. F. Mohammed, O. M. Bakr, P. Yang, P. Müller-Buschbaum, P. V. Kamat, Q. Bao, Q. Zhang, R. Krahne, R. E. Galian, S. D. Stranks, S. Bals, V. Biju, W. A. Tisdale, Y. Yan, R. L. Z. Hoye and L. Polavarapu, *ACS Nano*, 2021, **15**, 10775–10981.
26 S. K. Bera, S. Bera, M. Shrivastava, N. Pradhan and K. V. Adarsh, *Nano Lett.*, 2022, **22**, 8908–8916.

27 J.-N. Yang, T. Chen, J. Ge, J.-J. Wang, Y.-C. Yin, Y.-F. Lan, X.-C. Ru, Z.-Y. Ma, Q. Zhang and H.-B. Yao, *J. Am. Chem. Soc.*, 2021, **143**, 19928–19937.
28 S. Ghosh, B. Pradhan, W. Lin, Y. Zhang, L. Leoncino, P. Chabera, K. Zheng, E. Solano, J. Hofkens and T. Pullerits, *J. Phys. Chem. Lett.*, 2023, **14**, 1066–1072.
29 I. Cherniukh, G. Rainò, T. Stöferle, M. Burian, A. Travesset, D. Naumenko, H. Amenitsch, R. Erni, R. F. Mahrt, M. I. Bodnarchuk and M. V. Kovalenko, *Nature*, 2021, **593**, 535–542.
30 Y. Tang, L. Gomez, A. Lesage, E. Marino, T. E. Kodger, J.-M. Meijer, P. Kolpakov, J. Meng, K. Zheng, T. Gregorkiewicz and P. Schall, *Nano Lett.*, 2020, **20**, 5997–6004.
31 L. Protesescu, S. Yakunin, M. I. Bodnarchuk, F. Krieg, R. Caputo, C. H. Hendon, R. X. Yang, A. Walsh and M. V. Kovalenko, *Nano Lett.*, 2015, **15**, 3692–3696.
32 N. Pradhan, *Acc. Chem. Res.*, 2021, **54**, 1200–1208.
33 S. Bera, R. K. Behera and N. Pradhan, *J. Am. Chem. Soc.*, 2020, **142**, 20865–20874.
34 A. Garai, R. K. Behera and N. Pradhan, *J. Phys. Chem. C*, 2022, **126**, 16759–16766.
35 Z. Liu, Z. Hu, Z. Zhang, J. Du, J. Yang, X. Tang, W. Liu and Y. Leng, *ACS Photonics*, 2019, **6**, 3150–3158.
36 H. Zheng, J. Dai, J. Duan, F. Chen, G. Zhu, F. Wang and C. Xu, *J. Mater. Chem. C*, 2017, **5**, 12057–12061.
37 C. Zhang, J. Duan, F. Qin, C. Xu, W. Wang and J. Dai, *J. Mater. Chem. C*, 2019, **7**, 10454–10459.
38 O. H.-C. Cheng, T. Qiao, M. Sheldon and D. H. Son, *Nanoscale*, 2020, **12**, 13113–13118.
39 K. Wei, Z. Xu, R. Chen, X. Zheng, X. Cheng and T. Jiang, *Opt. Lett.*, 2016, **41**, 3821–3824.
40 R. Saran, A. Heuer-Jungemann, A. G. Kanaras and R. J. Curry, *Adv. Opt. Mater.*, 2017, **5**, 1700231.
41 S. Rudin, T. L. Reinecke and B. Segall, *Physical Review B*, 1990, **42**, 11218–11231.
42 K. Wu, A. Bera, C. Ma, Y. Du, Y. Yang, L. Li and T. Wu, *Phys. Chem. Chem. Phys.*, 2014, **16**, 22476–22481.
43 B. Ai, C. Liu, Z. Deng, J. Wang, J. Han and X. Zhao, *Phys. Chem. Chem. Phys.*, 2017, **19**, 17349–17355.
44 D. Baranov, S. Toso, M. Imran and L. Manna, *J. Phys. Chem. Lett.*, 2019, **10**, 655–660.
45 Y. Nagaoka, K. Hills-Kimball, R. Tan, R. Li, Z. Wang and O. Chen, *Adv. Mater.*, 2017, **29**, 1606666.
46 S. C. Boehme, M. I. Bodnarchuk, M. Burian, F. Bertolotti, I. Cherniukh, C. Bernasconi, C. Zhu, R. Erni, H. Amenitsch, D. Naumenko, H. Andrusiv, N. Semkiv, R. A. John, A. Baldwin, K. Galkowski, N. Masciocchi, S. D. Stranks, G. Rainò, A. Guagliardi and M. V. Kovalenko, *ACS Nano*, 2023, **17**, 2089–2100.
47 V. V. Temnov and U. Woggon, *Phys. Rev. Lett.*, 2005, **95**, 243602.